1   Phagocytic "teeth" and myosin-II "jaw" power target constriction during phagocytosis

2

3

4   Daan Vorselen[1*], Sarah R. Barger[2, 5*], Yifan Wang[3], Wei Cai[3], Julie A. Theriot[1], Nils C. Gauthier[4]
5   & Mira Krendel[2]

6

7

8   [1]Department of Biology and Howard Hughes Medical Institute, University of Washington,
9   Seattle, WA, 98195, USA

10   [2]Department of Cell and Developmental Biology, State University of New York Upstate Medical
11   University, Syracuse, NY, 13210, USA

12   [3]Department of Mechanical Engineering, Stanford University, Stanford, CA, 94305, USA

13   [4]IFOM, FIRC Institute of Molecular Oncology, Milan, 20139, Italy

14   [5]Current address: Molecular, Cellular, Developmental Biology, Yale University, New Haven, CT,
15   06511, USA

16

17   *These two authors contributed equally.

18   Correspondence: jtheriot@uw.edu and krendelm@upstate.edu

Abstract

Phagocytosis requires rapid actin reorganization and spatially controlled force generation to ingest targets ranging from pathogens to apoptotic cells. How actomyosin activity directs membrane extensions to engulf such diverse targets remains unclear. Here, we combine lattice light-sheet microscopy (LLSM) with microparticle traction force microscopy (MP-TFM) to quantify actin dynamics and subcellular forces during macrophage phagocytosis. We show that spatially localized forces leading to target constriction are prominent during phagocytosis of antibody-opsonized targets. This constriction is largely mediated by Arp2/3-mediated assembly of discrete actin protrusions containing myosin 1e and 1f ("teeth") that are interconnected in a ring-like organization. Contractile myosin-II activity contributes to late-stage phagocytic force generation and progression, suggesting a specific role in phagocytic cup closure. Observations of partial target eating attempts and sudden target release via a popping mechanism suggest that constriction may be critical for resolving complex *in vivo* target encounters. Overall, our findings suggest a phagocytic cup-shaping mechanism that is distinct from cytoskeletal remodeling in 2D cell motility and may contribute to mechanosensing and phagocytic plasticity.

Introduction

Phagocytic uptake of microbial pathogens, apoptotic cells, and debris are essential processes for human health[1,2]. Given the variety of phagocytic targets, ranging widely in shape, size and mechanical stiffness, this process requires remarkable plasticity. Phagocytosis is initiated when phagocytic receptors recognize distinct molecular patterns coating the target[3,4]. Downstream signalling from phagocytic receptors then leads to the formation of membrane protrusions, guided around the target through sequential ligand engagement in a zipper-like fashion[5–7], to make the phagocytic cup. Mechanically, progression of the phagocytic cup is powered by F-actin polymerization that pushes the plasma membrane forward and culminates in the eventual closure of the cup and the formation of a membrane-enclosed phagosome[8].

Previously, F-actin within the phagocytic cup was generally considered to be homogenous and the membrane extensions around the target were frequently likened to lamellipodia at the leading edge of a migrating cell[7,9–11]. Yet recent studies have identified dynamic adhesions or podosome-like structures within the phagocytic cup that appear to be sites of actin polymerization[12,13].

2

51 Podosomes are specialized F-actin adhesive structures that are prominent in myeloid cells and

52 capable of generating traction forces and degrading extracellular matrix[14,15]. This suggests a

53 fundamentally different mechanism for cup shaping (assembly of individual actin-based

54 protrusions vs. a uniform actin meshwork), and since podosomes are mechanosensitive[15–17], they

55 may contribute to the mechanosensitivity observed in phagocytosis, whereby phagocytes engulf

56 stiffer targets more readily than softer ones[8,18–21].

57 Moreover, the mechanism of cup closure and the involvement of myosin motor proteins therein

58 has remained elusive. Based on observations of phagocytes deforming red blood cells during

59 internalization[22–24], it has been hypothesized that closure of the phagocytic cup involves myosin-

60 II mediated "purse-string" contractility[25,26] However, the limited effect of myosin-II inhibition on

61 phagocytic uptake efficiency[27,28] and on traction forces tangential to the target surface has led to

62 the view that myosin-II likely does not contribute to phagocytic internalization[7].

63 It is clear that phagocytosis is driven by mechanical forces, but examining these forces has been

64 challenging due to the limitations of experimental approaches. Changes in cellular tension during

65 phagocytosis measured by micropipette aspiration have been well studied[29,30], but this technique

66 fails to capture cell-target forces and the spatial variation within the phagocytic cup. Recently,

67 traction force microscopy (TFM) combined with a 2D spreading assay known as frustrated

68 phagocytosis has been used to measure cell-target forces[12,20,25,31], however, this assay fails to

69 capture the biologically relevant geometry of the phagocytic cup, which very likely affects

70 cytoskeletal dynamics and force generation. Moreover, TFM only measures forces tangential to

71 the target surface, neglecting forces normal to the target surface, which may be critical. With the

72 recent introduction of particle-based force sensing methods[32,33], particularly microparticle traction

73 force microscopy (MP-TFM)[21], both normal and shear force components can now be studied

74 throughout phagocytosis.

75 Here, we utilize live-cell imaging combining MP-TFM and lattice light-sheet microscopy (LLSM)

76 to reveal how mechanical forces generated by actin polymerization and myosin contractility drive

77 phagocytic engulfment mediated by Fc receptors (FcRs). We show that phagocytes assemble F-

78 actin "teeth" that mediate target constriction throughout phagocytosis. Analysis of forces shows a

79 unique signature, in which target constriction, or squeezing, is balanced by pulling forces at the

80 base of the phagocytic cup at early stages and target compression throughout the cup at later

81 stages. Together, normal forces far exceed shear forces at the cell-target interface, pointing to a

82 mechanism fundamentally distinct from lamellipodial spreading in cell motility. We find that target

83 constriction is mediated by Arp2/3-mediated actin polymerization throughout phagocytosis.

84   Moreover, based on both force analysis and precise quantitative measurement of cup
85   progression, we establish a clear role for myosin-II purse string contractility, specifically in
86   phagocytic cup closure. Finally, we present how this force signature might be critical for target
87   selection and ingestion in more complex physiological settings.

88

89   **Results**

90   **Lattice light-sheet microscopy (LLSM) reveals sequence of target deformations induced**
91   **during live phagocytic engulfment**

92   Given the fast, 3D and light-sensitive nature of phagocytosis, we used lattice light-sheet
93   microscopy (LLSM) for high-speed volumetric imaging with minimal phototoxicity to investigate
94   cytoskeletal dynamics and phagocytic forces. To monitor internalization in real time, RAW264.7
95   macrophages were transfected with mEmerald-Lifeact for labelling of filamentous actin and were
96   fed deformable acrylamide-co-acrylic acid-microparticles (DAAMPs) (Fig. 1a). To investigate
97   FcR-mediated phagocytosis, DAAMPs were functionalized with BSA and anti-BSA IgG, as well
98   as AF647-Cadaverine for visualization[21] (Fig. 1b). RAW macrophages fed DAAMPs with a
99   diameter of 9 µm and a Young's modulus of 1.4 or 6.5 kPa typically formed a chalice-shaped
100   phagocytic cup and completed phagocytosis in similar timeframe (~3 minutes) as previously
101   reported for polystyrene particles[34] (Fig. 1a, Supplementary Video 1, Supplementary Fig. 1e). 3D
102   shape reconstructions of the DAAMPs enabled us to examine target deformations as a direct
103   readout of phagocytic forces in real time (Fig. 1b-c). Interestingly, we observed target constriction
104   defined by discrete spots of deformation that appeared around the circumference of the DAAMP
105   at the rim of the phagocytic cup (Fig. 1d, Supplementary Video 2). While these deformations were
106   more apparent using the softer 1.4 kPa DAAMPs, the same force pattern was observed using
107   stiffer 6.5 kPa targets (Supplementary Fig. 1a-b, Supplementary Video 3). These indentations
108   travelled parallel to the direction of phagocytic cup elongation, along the length of the DAAM
109   particle until cup closure and were associated with ~400 nm maximum target constriction for 1.4
110   kPa DAAMPs (Supplementary Fig. 1c). In addition, we observed bulk compression during
111   phagocytic cup progression (~ 0.5 kPa) and after complete internalization of the DAAMPs (up to
112   1.5 kPa), leading to a dramatic reduction in DAAMP diameter (Supplementary Fig. 1f-h). The
113   spherical appearance of targets and the gradual monotonic increase in compression after
114   completion of engulfment suggests that this compression may relate to the recently observed
115   shrinkage of internalized macropinosomes by osmotic pressure changes regulated by ion flux[35].
116   However, we sometimes observed the appearance of an F-actin shell around the target, similar

4

117 to previous reports[36], suggesting that cytoskeletal forces may also contribute to such compression

118 (Supplementary Fig. 1i, Supplementary Video 4).

119

120 **Forces normal to the target surface are dominant during phagocytic engulfment and lead**

121 **to strong target constriction**

122 To more closely investigate the role of the actin cytoskeleton in force generation during FcR-

123 mediated engulfment, we performed MP-TFM measurements on cells fixed during the process of

124 phagocytosis. RAW macrophages were exposed to 9 μm, 1.4 kPa DAAMPs, after which they

125 were fixed and stained for F-actin (Fig. 2a). Immunostaining of the exposed particle surface

126 allowed precise determination of the stage of engulfment (Supplementary Fig. 2a). Confocal Z-

127 stacks of phagocytic cups enabled 3D target shape reconstructions with super-resolution

128 accuracy and inference of cellular traction forces (Fig. 2b,c). The deformation patterns and

129 magnitudes for the fixed samples were similar to those observed in living cells by the LLSM

130 imaging of live cells (Fig. 2b, Supplementary Fig. 1d & 2b). Specifically, we noted a ring of

131 inhomogeneous F-actin localized along the rim of the phagocytic cup, where high F-actin intensity

132 strongly correlated with inward target deformation.

133 Force analysis revealed compressive stresses up to 400 Pa at these sites, which is substantially

134 greater than our previous findings of stresses of ~ 100 Pa using softer targets with Young's

135 modulus 0.3 kPa[21], and suggests that force exertion during phagocytosis may be regulated based

136 on target rigidity. The total compressive forces in the phagocytic rim, which lead to target

137 constriction, increased from ~ 1 nN in early-stage phagocytosis (fraction engulfed ~ 22%) to ~ 10

138 nN in later stages (fraction engulfed > 50%) (Fig. 2c). The shear forces (Fig. 2c) were consistent

139 in magnitude with reported values using TFM during frustrated phagocytosis on planar gels of

140 similar rigidity[31] and were ~7-fold lower than the observed normal forces, independent of the stage

141 of phagocytic engulfment (Fig. 2d). This suggests that normal forces dominate the mechanical

142 interaction in phagocytosis, which is in stark contrast with lamellipodial extension during cell

143 migration where shear forces dominate[37,38].

144

145

146

5

Target constriction coincides with the sites of F-actin accumulation and increases with uptake progression

To identify overall trends in F-actin distribution and location of target deformations within the phagocytic cup, we aligned the 3D images of phagocytic cups and analyzed profiles along the phagocytic axis, defined as the axis from the centroid of the cell-target contact area through the target centroid to the opposing target surface (Fig. 2e). This analysis confirmed a clear accumulation of F-actin near the front of the phagocytic cup (~ 5-fold higher than at the cup base), which precisely colocalized with the site of maximal applied inward normal forces regardless of engulfment stage, as illustrated by quantifying the surface mean curvature (Fig. 2f).

To investigate how phagocytic forces change during phagocytic progression, we arranged cups in order by the fraction of their particle surface engulfed, which allowed us to reconstruct phagocytic engulfment over time from fixed cell images (Fig. 2g, Supplementary Fig. 2b). Since DAAMPs cause little optical distortion, measurable features of the phagocytic cups could be analyzed independent of cup orientation and engulfment stage[21]. We found no marked accumulation of cups at any specific stage, suggesting no bottle-neck or rate-limiting steps, which had been previously reported around 50% engulfment[39]. However, we did observe a strong increase in global target deformation, measured as the inverse of target sphericity, with phagocytic progression (Spearman's ρ = -0.62, p = 5.0 × 10^{-8}) (Fig. 2h). This decrease in target sphericity was, at least partially, due to a 4 ± 1% (p = 1.9 × 10^{-7}) average increase in DAAMP elongation along the phagocytic axis (Fig. 2h), which is consistent with constriction in the direction orthogonal to the phagocytic axis. Direct analysis of target constriction and F-actin peak intensity for each phagocytic cup (Fig. 2i, Supplementary Fig. 6a) revealed an apparent contractile ring in almost all (~96%) of cups. The location of this actin contractile ring along the phagocytic axis correlated extremely well with phagocytic progression (ρ = 0.93, p = 3.2 × 10^{-29}) and led to target constriction increasing from ~80 nm in early-stage (fraction engulfed < 40%) to ~210 nm in late-stage cups (fraction engulfed >70%), which is a direct effect of increasing normal forces at the cup rim (Fig. 2j). Strikingly, in early stages of phagocytosis net pulling (or outward normal) forces were observed throughout the phagocytic cup and particularly at the base (~ 3 nN total force, > 100 Pa tensile stresses) (Fig. 2j), whereas in late-stage phagocytosis strong net compressive stresses were observed.

Arp2/3-mediated actin polymerization drives force generation throughout phagocytosis, whereas myosin-II powers cup closure

The striking observations of target constriction becoming more pronounced later in engulfment inspired us to consider distinct contributions of actin assembly and myosin-mediated contractility to force generation during phagocytosis. In order to separate the effects of these two actin-dependent processes, we inhibited Arp2/3-mediated and formin-mediated actin polymerization, as well as myosin-II activity using the small molecule inhibitors CK666, SMIFH2 and blebbistatin, respectively (Fig. 3a, Supplementary Fig. 3-5). Target deformation analysis and force calculations revealed that target constriction was strikingly diminished upon inhibition of the Arp2/3 complex and myosin-II activity, while formin inhibition had a relatively modest effect (Fig. 3c-d, Supplementary Fig. 6b, 6d). The loss of target constriction coincided with a strong reduction (~40%) in F-actin accumulation at the rim of the cup, as well as a 50% broadening of the typical narrow (~ 2 μm) F-actin band observed in the DMSO control (Fig. 3b,d,e, Supplementary Fig. 6c). Of note, upon myosin-II inhibition, the loss of F-actin at the rim of the cup was complemented by a small, but significant (p = 0.04), increase in F-actin density at the base of the cup (Fig. 3d,f). This observation suggests that myosin-II may be promoting actin disassembly at the base of the phagocytic cup during internalization, similar to the role of myosin-II in disassembling the F-actin network at the cell rear during cell motility[40].

We next investigated whether the activity of these molecular players may be associated with specific phagocytic stages. Our analysis revealed a significant change in the observed distribution of cup stages upon myosin-II inhibition, but not Arp2/3 or formin perturbation, compared to DMSO-treated control cells (Fig. 3g). Specifically, in the blebbistatin-treated cells, we found a > 6-fold enrichment of cups that were beyond 90% engulfment, but not yet closed (p = 1.9×10^{-4}). This high prevalence of late-stage phagocytic cups suggests a specific role for myosin-II in cup closure. Throughout phagocytosis, general particle deformations, as measured by the decrease in target sphericity, were strongly reduced upon both CK666 and blebbistatin treatment (Fig. 3h). Inhibition of formins generally reduced target deformations, but also increased the cell-to-cell variability in particle deformation, suggesting that formins may play a role in fine-tuning phagocytic force production (Fig. 3h). Whereas overall target deformations were reduced in all stages of phagocytosis upon Arp2/3 inhibition, myosin-II inhibition only significantly affected phagocytic force generation at later stages, after 50% engulfment (Fig. 3h). A similar effect was observed when quantifying target constriction specifically (Fig. 3i). Thus, in contrast to the prevailing view

7

210   that myosin-II is dispensable for phagocytosis[7, 27,28], this analysis strongly suggests that there is

211   a specific role for myosin-II in contributing to the efficiency of late-stage phagocytosis.

212

Actin-based protrusive teeth drive target constriction and are mechanosensitive

214   Based on our observations of discrete spots of inward deformation using MP-TFM (Fig. 1a,b, Fig.

215   2a,b), and the significant reduction in target deformation after treatment of cells with the Arp2/3

216   inhibitor CK666, we hypothesized that these local deformations were the result of actin-based

217   protrusions pushing against the surface of the phagocytic target. Indeed, we frequently observed

218   actin rich puncta that appeared as oblong or triangular tooth-like projections locally indenting the

219   target surface along the internal rim of the phagocytic cup (Fig. 4a) and sometimes deeper within

220   the cup (Fig. 4b). Similar actin "teeth" were formed by primary murine bone-marrow derived

221   macrophages (BMDM), bone marrow-derived dendritic cells (BMDC) and HL-60 human

222   neutrophils when challenged with IgG-functionalized DAAMPs, suggesting that these structures

223   are a common feature of phagocytosis (Fig. 4c).

224   To investigate the nature and biological function of these actin "teeth" more carefully, we identified

225   them on individual particles based on their protrusive nature and high F-actin intensity

226   (Supplementary Fig. 7a,b). According to these criteria, teeth were found in almost all phagocytic

227   cups, with ~10 distinct teeth per cup (Fig. 4d). Typically ~1 μm in diameter, and protruding ~200

228   nm into the 1.4 kPa DAAMP targets, they resembled podosomes in size and protrusive nature[16].

229   Cells treated with the Arp2/3 inhibitor CK666, and to a lesser extent cells treated with the formin

230   inhibitor SMIFH2, exhibited a reduction in the number of actin teeth per cup (80% and 40%

231   reduction, respectively) compared to control cells treated with DMSO (Fig. 4d). This result

232   suggests that, like podosomes[17], target-deforming phagocytic teeth include both Arp2/3- and

233   formin-nucleated actin filaments. Surprisingly, a strong decrease (~50%) in the number of actin

234   teeth was also observed upon myosin-II inhibition. For all treatments, the reduced number of

235   individual teeth that still formed were remarkably similar to those formed by control cells. Although

236   tooth size and depth were reduced upon CK666 or blebbistatin treatment, the effect size was

237   small (< 15%), suggesting that "teeth" are resilient structures that, once formed, have well-defined

238   properties (Fig. 4d).

239   LLSM allowed us to track the dynamics of actin teeth during phagocytosis (Fig. 4e), which

240   revealed clear forward movement over the target surface. A few teeth that we initially detected

241   near the rim stayed in place, remaining where they had assembled during early-stage

242   phagocytosis, suggesting that teeth located deeper within the phagocytic cup (as observed in the

243   fixed cell images) may have originated earlier from the cup rim and been left behind as the cup

244   progressed (Fig. 4b, Supplementary Fig. 7e). More commonly, however, teeth moved forward

245   with a speed of ~5.6 μm/min, similar to the previously reported values for podosome-like

246   structures on very stiff substrates during frustrated phagocytosis[41]. Strikingly, teeth within the

247   same phagocytic cup appeared to move in a coordinated fashion, with similar speed and direction,

248   and even with observed collective speed changes (Fig. 4e, Supplementary Fig. 7d). This suggests

249   that phagocytic teeth, like podosomes[42,43], are mechanically interlinked at the mesoscale.

250   To test whether the actin teeth were mechanosensitive, we challenged RAW macrophages to

251   ingest 9 μm DAAMPs of 1.4 or 6.5 kPa and fixed and stained cells to examine actin teeth

252   formation. Interestingly, RAW macrophages assembled actin teeth more frequently when fed

253   softer targets (Fig. 4i), suggesting that phagocytic teeth may play a role in the overall

254   mechanosensitivity of phagocytosis[8,18–21].

255   Given the ring-like organization of phagocytic teeth in the cup rim, combined with their individual

256   protrusive activity, we questioned whether they were sufficient to explain our observations of

257   target constriction orthogonal to the phagocytic axis, or if a separate contractile mechanism is

258   required. We first distinguished the teeth positioned at the rim of the cup (~70% of teeth), which

259   likely contribute to target constriction, from those deeper in the cup, based on their distance from

260   the cup rim (Fig. 4f, Supplementary Fig. 7c). We then determined whether the properties of teeth

261   near the rim correlated with the overall target constriction. Indeed, the number of teeth per cup

262   and tooth size correlated with overall constriction in DMSO treated cells and between groups

263   treated with actomyosin activity inhibitors CK666, SMIFH2 and Blebbistatin (Fig. 4g,

264   Supplementary Fig. 7f). We further examined whether changes in the teeth could be related to

265   increasing target constriction with phagocytic cup progression. Teeth numbers increased only

266   slightly with phagocytic progression, which suggests that they are formed quickly early on in

267   phagocytosis and are then typically maintained at constant numbers throughout engulfment (Fig.

268   4h). Teeth size and depth increased significantly but modestly during phagocytic progression (Fig.

269   4h, Supplementary Fig. 7g). Elasticity theory simulations of teeth-like indentations of a spherical

270   target allowed us to test whether teeth protrusive activity is sufficient to explain the extent of

271   overall target constriction in different stages of phagocytosis (Supplementary Fig. 8).

272   Remarkably, this revealed that teeth activity is indeed sufficient to account for total target

273   constriction in early-stage phagocytosis (< 50% engulfment), but insufficient to explain the greater

274   degree of target constriction later in the process (Fig. 4j). This is consistent with additional myosin-

275   II based contractile forces in late-stage phagocytosis, as suggested by our observations using

276   Blebbistatin.

277

278   Regulators of branched actin assembly (Arp2/3 and WASP) and myosin-I isoforms

279   localize to actin teeth while myosin-II forms contractile rings within the phagocytic cup

280   Due to the resemblance of the phagocytic actin teeth to podosomes in size, protrusive activity

281   (Fig. 4d) and dynamics (Fig. 4e), we naturally questioned whether these structures were similar

282   in protein composition as well. Given technical challenges with immunohistochemical staining and

283   MP-TFM (see methods), we transfected the RAW macrophages with fluorescently tagged

284   proteins to assess tagged protein localization relative to the actin teeth using 3D reconstructions

285   of the DAAMP (Fig. 5a-b). Consistent with our earlier results showing a decrease in the number

286   of teeth after treating cells with the Arp2/3 inhibitor, we found that the Arp2/3 complex and its

287   activator, WASP, colocalized with the actin teeth. Moreover, cortactin and cofilin, actin-binding

288   proteins that are frequently found in association with densely branched actin networks, also

289   localized to the phagocytic teeth (Supplementary Fig. 9a). In contrast, myosin-II often appeared

290   distinctly behind the actin teeth in an anti-correlated fashion (Fig. 5b). In particular, rings

291   composed of myosin-II filaments could be seen within the phagocytic cup (Fig. 5a). In phagocytic

292   cups that were further along the engulfment process, myosin-II coalesced into a ring behind the

293   actin rim (Supplementary Fig. 9b) and clearly localized at sites of target constriction in cases of

294   extreme target deformation (Fig. 5c). Meanwhile, the two long-tailed myosin-I isoforms, myo1e

295   and myo1f, localized specifically to the tips of the actin teeth, consistent with our previous

296   observations (Fig. 5a)[12]. Two formins tested, mDia2 and FHOD1, did not localize to phagocytic

297   actin teeth (Supplementary Fig. 9c).

298   Given both recent and older observations identifying adhesion adaptor proteins at the phagocytic

299   cup[18,44], we were particularly interested in the localization of paxillin and vinculin. In comparison

300   to the branched actin-binding proteins, both paxillin and vinculin localized behind the phagocytic

301   teeth in a punctate-like pattern (Supplementary Fig. 9d). Altogether, these studies support a

302   model where the actin teeth are composed of branched actin filaments guided by myosin-I motor

303   proteins. The localization of myosin-II and paxillin/vinculin behind the teeth suggests that these

304   proteins may contribute to the mechanical interconnection of the teeth, similar to podosomes on

305   2D surfaces[17,43].

306

Contractile activity may enable resolution of phagocytic conflicts via partial target eating ("nibbling") or forfeit of uptake ("popping")

While we have found that target constriction is a signature mechanical feature of FcR-mediated phagocytic progression, it is unclear what functional role target constriction might play during phagocytosis, since actin-driven membrane advancement along the target surface should in principle be sufficient for internalization[45,46]. In addition to the many successful internalization events we observed using LLSM, we also observed some strikingly different target encounters in which RAW macrophages assembled large amounts of F-actin, only to squeeze futilely at the base of the target without completing engulfment. In these cases, the contractile activity resulted in dramatic deformations and even dumbbell-like appearance of the target (Fig. 6a,b, Supplementary Video 5). In addition to this kind of internalization failure by single cells, we also observed incidents where two macrophages engaged one DAAMP target. Similar to previous observations of red blood cells (RBCs) being squeezed into multilobed shapes when attacked by two macrophages simultaneously[22], these conflicts were also observed using primary BMDMs challenged with DAAMPs (Supplementary Video 6). Although the polymeric targets used in this study prohibit partial target eating because each particle is effectively one single crosslinked macromolecule that cannot easily be severed by cell-scale forces, this behavior may be reminiscent of trogocytosis, the process which has been observed during immune cell attack of cancer cells whereby phagocytes ingest small bits of their target[47–49]. By imaging RAW macrophages transfected with GFP-NMMIIA, we observed highly enriched rings of myosin-II signal at DAAMP deformations during attempts of partial target eating (Fig. 6c, Supplementary Video 7). Target encounters involving extreme deformations of the DAAMP also revealed the existence of a "popping" mechanism that could lead to a sudden release of the target (Supplementary Video 8) or, conversely, a sudden completion of engulfment (Supplementary Video 9, Supplementary Fig. 10). During such events, targets were first gradually deformed to a dumbbell-like shape, followed by a sudden translocation of the particle, as well as an immediate recovery of its original spherical shape and volume (Fig. 6d, Supplementary Video 7). The rapid timescale of this process suggests that it is likely purely mechanical, representing an elastic recoil of the DAAMP. Importantly, these encounters were rather common, with the attempted partial eating attempts (~14%) and popping (~24%) making up almost 40% off all recorded events (Fig. 6e). Furthermore, such events, and specifically popping, were mechanosensitive and occurred much less frequently for stiffer 6.5 kPa targets (~1%, n = 89, $p = 1.5 \times 10^{-6}$), resulting in the overall more frequent failure of phagocytosis for soft particles (Fig. 6f).

Discussion

Through the combination of LLSM and MP-TFM, we report here a detailed analysis of the mechanical progression of phagocytosis and the contributions of several key molecular players. Most importantly, we have discovered that FcR-mediated phagocytosis occurs through a unique mechanism in which normal forces dominate over shear forces in the cell-target interaction. This is in contrast to the current view that the phagocytic cup is equivalent to the leading edge of a migrating cell, where shear forces typically predominate at the cell-substrate interface[37,38]. In addition, the fast forward movement of actin teeth, which underlie target constriction, concomitant with phagocytic cup progression across the target is in stark contrast to lamellipodial focal adhesion complexes (FAs), which are fixed relative to the substratum[38]. The strong target constriction recently observed in complement-mediated phagocytosis by peritoneal macrophages *in vitro*[50], and in phosphatidylserine-mediated phagocytosis by epithelial cells in zebrafish embryos[51] suggests that strong normal forces and target constriction are likely a general feature of phagocytosis.

We show that normal forces are primarily generated by protrusive phagocytic actin "teeth" and myosin-II contractility, which make distinct contributions to target constriction. While actin-based puncta have been previously observed during phagocytosis of stiffer polystyrene beads[12,13], their presence in multiple phagocytic cell types (Fig. 4c) suggests a common role in phagocytosis. These structures are podosome-like in protein composition, consisting of mostly branched F-actin and actin regulatory proteins. Accordingly, inhibition of the Arp2/3 complex dramatically reduces tooth number and size and consequently reduces target constriction. Unexpectedly, myosin-II motor inhibition also reduces tooth number and size, albeit to a lesser extent than Arp2/3 inhibition, and also alters tooth spatial distribution (Supplementary Fig. 7c). In podosomes, myosin-II filaments interconnect radial actin fibers of individual podosomes to create a coherent network[43]. The localization of myosin-II behind and in between teeth, as well as the coordinated movement of teeth, suggests that actin teeth in phagocytosis are similarly interconnected by actomyosin structures. This molecular arrangement of actin teeth (Fig. 7a) bears similarity to the organization of podosome rosettes[14], and we show that they possess a similar mechanosensitivity (Fig. 4j)[15–17]. We find that individual teeth grow larger and stronger with phagocytic progression, correlating with increasing myosin-II constriction observed in late-stage phagocytosis (Fig. 7a). These observations may relate to the force feedback mechanism observed in Arp2/3 mediated branched actin networks *in vitro* showing that mechanical resistance makes self-assembling actin networks stronger[52]. Thus, increased myosin-II contraction in late-stage phagocytosis may

12

373   promote stronger actin teeth. This rapid structural reinforcement by myosin-II has not been

374   described for actin cores of podosomes on 2D, making this feature unique to phagocytosis.

375   We further show that myosin-II plays an important role in phagocytic cup closure – a stage in

376   phagocytosis that has been notoriously difficult to study experimentally[53] (Fig. 7a). Generally,

377   myosin-II is not deemed important for cup closure or phagocytic progression[7,22], yet we observe

378   myosin-II enrichment at the rim of phagocytic cups (Fig. 5c). Moreover, blebbistatin treatment

379   specifically affects late-stage contractile force generation (Fig. 3h) causing cup closure to become

380   a bottle-neck step as evidenced by the accumulation of late-stage phagocytic cups (Fig. 3g).

381   Because these forces are exerted normal to the target surface, the contribution of myosin-II

382   activity to phagocytic progression has likely gone unnoticed in previous studies using regular TFM

383   on a planar substrate, which only measures forces that are tangential to the surface (shear)[12,20,25].

384   We show that phagocytosis is hallmarked by a unique force balance, where before 50%

385   engulfment, target constriction results in an outward force balanced by pulling forces throughout

386   the base of the phagocytic cup (Fig. 7b). Given the reduced presence of cytoskeletal components

387   at the base of the cup (Supplementary Fig. 2b)[4,7], these pulling forces are most likely not due to

388   actin polymerization forces or actomyosin contractility, but instead a result of the target being held

389   in place through receptor-ligand bonds throughout the base of the cup. Hence, the forces acting

390   on receptor-ligand bonds within the cup are likely dependent on the target physical properties and

391   the local geometry at the rim of the cup (Fig. 7b). Since the lifetime of such bonds is tension-

392   dependent[54,55], this push-and-lock mechanism may enable sensing of physical target properties

393   through a proofreading mechanism and thereby aid macrophages in target selection. Indeed, we

394   observe that forfeit of uptake via popping, in which the outward-directed forces likely overcome

395   the strength of the receptor-ligand interactions, depends on the local target geometry and target

396   rigidity. In addition, for non-spherical targets (e.g. ellipsoidal), this force balance would result in a

397   net torque aligning the target's long axis along the phagocytic axis, which has been observed

398   previously and is reported to lead to enhanced uptake efficiency of ellipsoidal targets[19,56,57].

399   We observed that actin teeth formed more frequently when cells were challenged with softer

400   targets, yet we also associated softer targets with more instances of failed internalization. This

401   calls into question the effectiveness of actin teeth, and, more generally, target constriction, in

402   driving phagocytic internalization. Aside from a role in cup closure, target constriction could be

403   important for creating a tight apposition between the cell and target, which is essential for receptor

404   engagement[58]. Surprisingly though, we noticed that overly strong target constriction leads to

405   failure of attempted phagocytosis, expressed either as partial eating or a popping mechanism

13

406   leading in forfeit of uptake. Although these mechanisms may lead to reduced uptake efficiency in

407   isolated phagocyte-target interaction, we suspect they may be critical in more complex phagocytic

408   encounters that occur *in vivo*, *e.g.* when multiple macrophages approach a single target (Fig. 6g),

409   or attempt to engulf adherent and hard-to-reach targets[8,11,59]. Altogether, our findings show that

410   actin polymerization-dependent protrusive forces and myosin-II-dependent contractile forces

411   contribute to driving target deformation and phagocytic internalization, and likely both participate

412   in the mechanosensation required for phagocytic plasticity.

Code availability

The Matlab code for analysing confocal images and deriving particle shape is publicly available on https://gitlab.com/dvorselen/DAAMparticle_Shape_Analysis. The Python code used for analysing tractions is provided on https://gitlab.com/micronano_public/ShElastic.

Author Contributions

S.R.B., D.V., N.C.G., J.A.T. and M.K. conceived of and designed the study. S.R.B performed experiments and D.V. generated reagents, wrote the image analysis software and analyzed the data. Y.W. and W.C. performed the force analysis. J.A.T., N.C.G. and M.K. supervised the project. S.R.B., D.V., N.C.G., J.A.T., and M.K. wrote the manuscript.

Declaration of Interests

The authors declare no conflicts of interest.

438 **Methods**

439

440 **Cell culture**

441 RAW264.7 (ATCC; male murine cells) were cultured in DMEM, high glucose, containing 10% FBS

442 and 1% antibiotic-antimycotic (Gibco) (cDMEM) at 37 °C with 5% CO_2. HL-60 cells (ATCC; CCL-

443 240) were cultured in RPMI plus L-glutamine supplemented with 20% FBS and 1% antibiotic-

444 antimycotic (cRPMI). HL-60 cells were differentiated into neutrophil-like cells in culture media

445 containing 1.5% DMSO and used at day 5-6 post-differentiation and plated on 20 μg/mL

446 fibronectin. For the collection of primary murine bone marrow progenitor cells, femurs and tibias

447 of C57BL/6 mice were removed and flushed with cDMEM. Red blood cells were lysed using ACK

448 buffer (0.15 M NH_4Cl) and bone marrow progenitor cells were recovered by centrifugation (250×g,

449 5 min, 4 °C), washed once with sterile PBS and plated on tissue culture dishes in cDMEM at 37 °C

450 with 5% CO_2. For differentiation into bone-marrow derived macrophages (BMDM), non-adherent

451 cells were moved to bacteriological Petri dishes the next day and differentiated over 1 week in

452 cDMEM containing 20 ng/mL recombinant murine M-CSF (Biolegend, 576404). Generation of

453 murine bone-marrow derived dendritic cells (BMDC) has been previously described[60]. In brief,

454 bone marrow progenitor cells were collected in cRPMI and replated in cRPMI containing 20 ng/mL

455 recombinant murine GM-CSF (Peprotech, 315-03) (DC media). On day 3, DC media was

456 supplemented. On days 6 and 8, half of the culture supernatant and nonadherent cells were spun

457 down and resuspended in cRMPI containing 5 ng/mL GM-CSF. DC maturation was assessed on

458 day 10 by flow cytometry using PE-Cd11c (Biolegend, 117307) and FITC-MHC-II (Biolegend,

459 107605) staining. Cells were used on Day 12. All procedures utilizing mice were performed

460 according to animal protocols approved by the IACUC of SUNY Upstate Medical University and

461 in compliance with all applicable ethical regulations.

462

463 **Chemicals and drugs**

464 Blebbistatin, CK-666, and SMIFH2, and fibronectin were purchased from EMD Millipore. Alexa

465 Fluor-488, Alexa Fluor-568, Alexa Fluor-647 conjugated phalloidin were purchased from Life

466 Technologies. Janelia Fluor 549 (JF549) HaloTag Ligand was a generous gift from Luke Lavis.

467

468

16

Constructs and transfection

Human myo1e and myo1f constructs tagged with EGFP, mEmerald-C1, or mScarlet-C1 have been previously described[12]. mEmerald-Lifeact was a gift from Michael Davidson (Addgene #54148). Chicken regulatory light chain (RLC) tagged with EGFP was a gift from Klaus Hahn. WASP tagged with myc was a gift from Dianne Cox, and was subcloned into pUB-Halo-C1 vector. CMV-GFP-NMHCII-A was a gift from Robert Adelstein (Addgene #11347). ARP3-mCherry (Addgene #27682) and mCherry-cortactin (Addgene #27676) were gifts from Christien Merrifield that were subcloned into EGFP-C1 and mEmerald-C1, respectively. Chicken paxillin was a gift from Chris Turner, which was subcloned into mScarlet-i-C1. Chicken vinculin was a gift from Kenneth Yamada (Addgene #50513) and subcloned into pUB-mEmerald-C1. Immunohistochemical staining to determine localization of select podosome-related proteins in relation to the actin teeth did not produce good results, which may be due to the adhesive and porous nature of the IgG-functionalized DAAMPs. As an alternative, we transfected the RAW macrophages with fluorescently tagged proteins. All transfections were accomplished by electroporation (Neon) using the manufacturer's instructions.

Microparticle synthesis

DAAM-particles were synthesized as previously described[21]. First, acrylamide mixtures containing 100 mg/mL acrylic components, 150 mM NaOH, 0.3% (v/v) tetramethylethylenediamine (TEMED), 150 mM MOPS (prepared from MOPS sodium salt, pH 7.4) were prepared. Mass fraction of acrylic acid was 10% and crosslinker mass fraction was 0.65% or 2.3%, for 1.4 kPa and 6.5 kPa particles, respectively. Prior to extrusion, the gel mixture was degassed for 15 minutes and then kept under nitrogen atmosphere until the extrusion process was complete. Tubular hydrophobic Shirasu porous glass (SPG) were sonicated under vacuum in n-heptane, mounted on an internal pressure micro kit extruder (SPG Technology Co.) and immersed into the oil phase (~125 mL) consisting of hexanes (99%) and 3% (v/v) Span 80 (Fluka, 85548 or Sigma-Aldrich, S6760). 10 mL of gel mixture was extruded through SPG membranes under nitrogen pressure of approximately 7 kPa, 15 kPa, for membranes with pore size 1.9 μm and 1.4 μm, respectively. 9 mm, 1.4 kPa particles were synthesized using 1.4 μm pore size membranes, whereas 9 μm, 6.5 kPa particles and 11 μm, 1.4 kPa particles were made using 1.9 μm pore size membranes. The oil phase was continuously stirred at 300 rpm and kept under nitrogen atmosphere. After completion of extrusion, the emulsion temperature was increased to 60 °C and

17

501   polymerization was induced by addition of ~225 mg 2,2'-Azobisisobutyronitrile (AIBN) (1.5 mg/mL

502   final concentration). The polymerization reaction was continued for 3 h at 60 °C and then at 40

503   °C overnight. Polymerized particles were subsequently washed (5x in hexanes, 1x in ethanol),

504   dried under nitrogen flow for approximately 30 minutes, and resuspended in PBS (137 NaCl, 2.7

505   mM KCl, 8.0 mM Na_2HPO_4, 1.47 mM KH_2PO_4, pH 7.4) and stored at 4 °C.

506

Microparticle functionalization

508   DAAM-particles were functionalized as previously described[21]. In brief, DAAMPs were diluted to

509   5% (v/v) concentration and washed twice in activation buffer (100 mM MES, 200 mM NaCl, pH

510   6.0). They were then incubated for 15 min in activation buffer supplemented with 40 mg/mL 1-

511   ethyl-3-(3-dimethylaminopropyl) carbodiimide, 20 mg/mL N-hydroxysuccinimide (NHS) and 0.1%

512   (v/v) Tween 20, while rotating. Afterwards they were spun down (16,000 x g, 2 min) and washed

513   4X in PBS, pH 8 (adjusted with NaOH) with 0.1% Tween 20. Immediately after the final wash the

514   particles were resuspended in PBS, pH 8 with BSA (Sigma, A3059) and incubated, rocking for 1

515   h. Then cadaverine-conjugate was added: either Alexa Fluor 488 Cadaverine (Thermo Fischer

516   Scientific, A-30679) or Alexa Fluor 647 Cadaverine (Thermo Fischer Scientific, A-30676) to a final

517   concentration of 0.2 mM. After 30 min, unreacted NHS groups were blocked with 100 mM TRIS;

518   100 mM ethanolamine (pH 9). DAAM-particles were then spun down (16,000 x g, 2 min) and

519   washed 4X in PBS, pH 7.4 with 0.1% Tween 20. Finally, BSA-functionalized DAAMPs were

520   resuspended in PBS, pH 7.4 without Tween.

521

Phagocytosis assay

523   DAAM particles were washed 3X in sterile PBS and opsonized with rabbit anti-BSA antibody (MP

524   Biomedicals, 0865111) for 1 h at room temperature. DAAMPs were then washed three times

525   (16000 x g, 2 min) with PBS and resuspended in sterile PBS. DAAM particles were added to a

526   total volume of 400 µl of serum-free DMEM, briefly sonicated in a bath sonicator, and applied to

527   phagocytes in a 12-well plate. To synchronize phagocytosis and initiate DAAMP-phagocyte

528   contact, the plate was spun at 300 × *g* for 3 min at 4°C. Cells were incubated at 37°C to initiate

529   phagocytosis for a period of 3-5 min. Media was then removed and cells were fixed with 4%

530   PFA/PBS for 15 min. Any unbound DAAMPs were then washed away with 3X washes of PBS and

531   cells were stained with goat anti-rabbit-Alexa Fluor-405 antibodies (Invitrogen, A31556, 1:400) for

532   30 min to visualize exposed DAAM area. Cells were then washed with PBS (3 × 5 min) and

533   permeabilized with 0.1% Triton X-100/PBS for 3 min, then stained with Alexa Fluor-568 or -488

534   conjugated phalloidin (1:300). Coverslips were then mounted using VECTASHIELD Antifade

535   Mounting Medium (Vector Laboratories, H-1000) and sealed with nail polish. For drug treatments,

536   cells were exposed to the indicated drug concentration for 30 min prior to the assay and DAAM

537   particles were resuspended and exposed to cells in the same drugged media.

538

Microscopy

540   Confocal images were taken using a PerkinElmer UltraView VoX Spinning Disc Confocal system

541   mounted on a Nikon Eclipse Ti-E microscope equipped with a Hamamatsu C9100-50 EMCCD

542   camera, a 100 × (1.4 N.A.) PlanApo objective, and controlled by Volocity software. Images for

543   protein localization were taken using a Leica TCS SP8 laser scanning confocal microscope with

544   a HC Pl APO 63×/1.4 NA oil CS2 objective at Upstate/Leica Center of Excellence for Advanced

545   Light Microscopy. Confocal image data were less prone to artifacts than the LLSM images

546   (Supplementary Fig. 1j), and therefore chosen for accurate force analysis.

547   The lattice light-sheet microscope[61] utilized was developed by E. Betzig and operated/maintained

548   in the Advanced Imaging Center at the Howard Hughes Medical Institute Janelia Research

549   Campus (Ashburn, VA). 488, 560, or 642 nm diode lasers (MPB Communications) were operated

550   between 40 and 60 mW initial power, with 20–50% acousto-optic tunable filter (AOTF)

551   transmittance. The microscope was equipped with a Special Optics 0.65 NA/3.75 mm water

552   dipping lens, excitation objective and a Nikon CFI Apo LWD 25 × 1.1 NA water dipping collection

553   objective, which used a 500 mm focal length tube lens. Live cells were imaged in a 37 °C-heated,

554   water-coupled bath in FluoroBrite medium (Thermo Scientific) with 0–5% FBS and Pen/Strep.

555   Images were acquired with a Hamamatsu Orca Flash 4.0 V2 sCMOS cameras in custom-written

556   LabView Software. Post-image deskewing and deconvolution was performed using HHMI Janelia

557   custom software and 10 iterations of the Richardson-Lucy algorithm.

558

Microparticle 3D shape reconstruction and force analysis

560   Image analysis was performed with custom software in Matlab, similar to described previously[21].

561   Briefly, images were thresholded to estimate the volume and centroid of individual microparticles.

562   Cubic interpolation was then used to calculate the intensity values along lines originating from the

19

563 particle centroid and crossing the particle edge. Edge coordinates were then directly localized

564 with super-resolution accuracy by fitting a Gaussian to the discrete derivative of these line profiles.

565 This is significantly faster than using pre-processing of the image stacks with the 3D Sobel

566 operator as used previously[21]. Before calculation of particle properties, such as sphericity, relative

567 elongation and surface curvature, as well as traction forces, edge coordinates were smoothed

568 using the equivalent of a 2D moving average for a spherical surface, operating on the radial

569 component of the edge coordinates. Great circle distances (d) between edge coordinates with

570 indices i and j were calculated along a perfect sphere: $d = \arccos\left(\sin\theta_i \sin\theta_j + \right.$

571 $\left. \cos\theta_i \cos\theta_j \cos(\varphi_i - \varphi_j)\right) R$, where R is the equivalent radius of a sphere to the particle. The radial

572 component of the edge coordinates was then averaged within the given window size (1 μm^2). A

573 triangulation between edge coordinates was generated, and the particle surface area S and

574 volume V calculated. Sphericity was calculated as $\Psi = (6\pi^{1/3}V^{2/3}S^{-1})$. For surface curvature

575 calculations, first principal curvatures (k_1 and k_2) of the triangulated mesh were determined as

576 described previously[62,63]. The mean curvature was calculated $H = (k_1 + k_2)/2$. Force calculations

577 were performed using the spherical harmonics method within custom Python package ShElastic

578 as described in detail previously[21,64]. Chosen values for the weighing parameter α for residual

579 traction and β for anti-aliasing were both 1.

580

Fluorescent mapping on particle surface and determination of fraction engulfed

582 Mapping of fluorescent proteins, phalloidin and immunostaining to the particle surface was done

583 by determination of the fluorescent intensity along radial lines originating from the particle centroid

584 and passing through each edge coordinate (Fig. 1c). Linear interpolation was used to determine

585 the intensity along each line, and the maximum value within a 1 μm distance of the edge

586 coordinate was projected onto the surface. The calculation of the fraction engulfed, alignment of

587 particles using the centroid of the contact area, and obtaining of a stress-free boundary for force

588 calculations was done as described previously[21], with the exception that here both the phalloidin

589 stain and the immunostaining of the free particle surface were used to determine the mask

590 (Supplementary Fig. 2a). For LLSM data, where no staining of the free particle surface was

591 present, alignment was done manually.

592

593

20

Indentation simulations:

Indentation simulations of teeth on a spherical target particle were based on the Hertz contact model[65]. Parameters of the model were estimated from experimental data: the undeformed radius of the target particle was set at $R_{\text{target}} = 3.7\mu$m; the teeth are considered as rigid spherical indenters with radius $R_{\text{teeth}} \approx 0.5$ μm; and 10 teeth were simulated for each target, which were equally distributed around the equator of the target sphere (Supplementary Fig. 8a). The force F and the contact area radius a produced by indentation to absolute depth d for each individual indenter were then evaluated:

$$F = \frac{4}{3}E^*R^{*\frac{1}{2}}d^{\frac{3}{2}}, \qquad a = \sqrt[3]{\frac{3FR^*}{4E^*}},$$

where the effective Young's modulus E^* and effective radius R^* are

$$\frac{1}{E^*} = \frac{1 - v_{\text{tooth}}^2}{E_{\text{tooth}}} + \frac{1 - v_{\text{target}}^2}{E_{\text{target}}} = \frac{3}{4E_{\text{target}}}, \qquad \frac{1}{R^*} = \frac{1}{R_{\text{teeth}}} + \frac{1}{R_{\text{target}}}$$

given that the target particle is near incompressible ($v_{target} = 0.5$) and the teeth are rigid compared to the target (E_{tooth} >> E_{target}). Considering non-friction contact, the force distribution on the target sphere in the contact area of each tooth can be written as,

$$p(r) = p_0\sqrt{1 - \left(\frac{r}{a}\right)^2}, \qquad p_0 = \frac{3F}{2\pi a^2}, \qquad r \in [0, a],$$

where r is the radius to the initial contact point, and p_0 is the maximum pressure on the contact plane. Given the resulting traction force map $T(\theta, \varphi)$ as the boundary condition on the target sphere surface, we solved the elasticity problem, and obtained the displacement map $u(\theta, \varphi)$ using our ShElastic package (Supplementary Fig. 8b)[64] . The (θ, φ) map on the spherical surface has the size of 61x121, which is defined by Gauss-Legendre quadrature[66]. Simulations were carried out for a range of tooth radii R_{teeth} and absolute depth d to obtain the effective tooth depth and the average constriction along the equator (Supplementary Fig. 8b), which are directly comparable with experimentally obtained data.
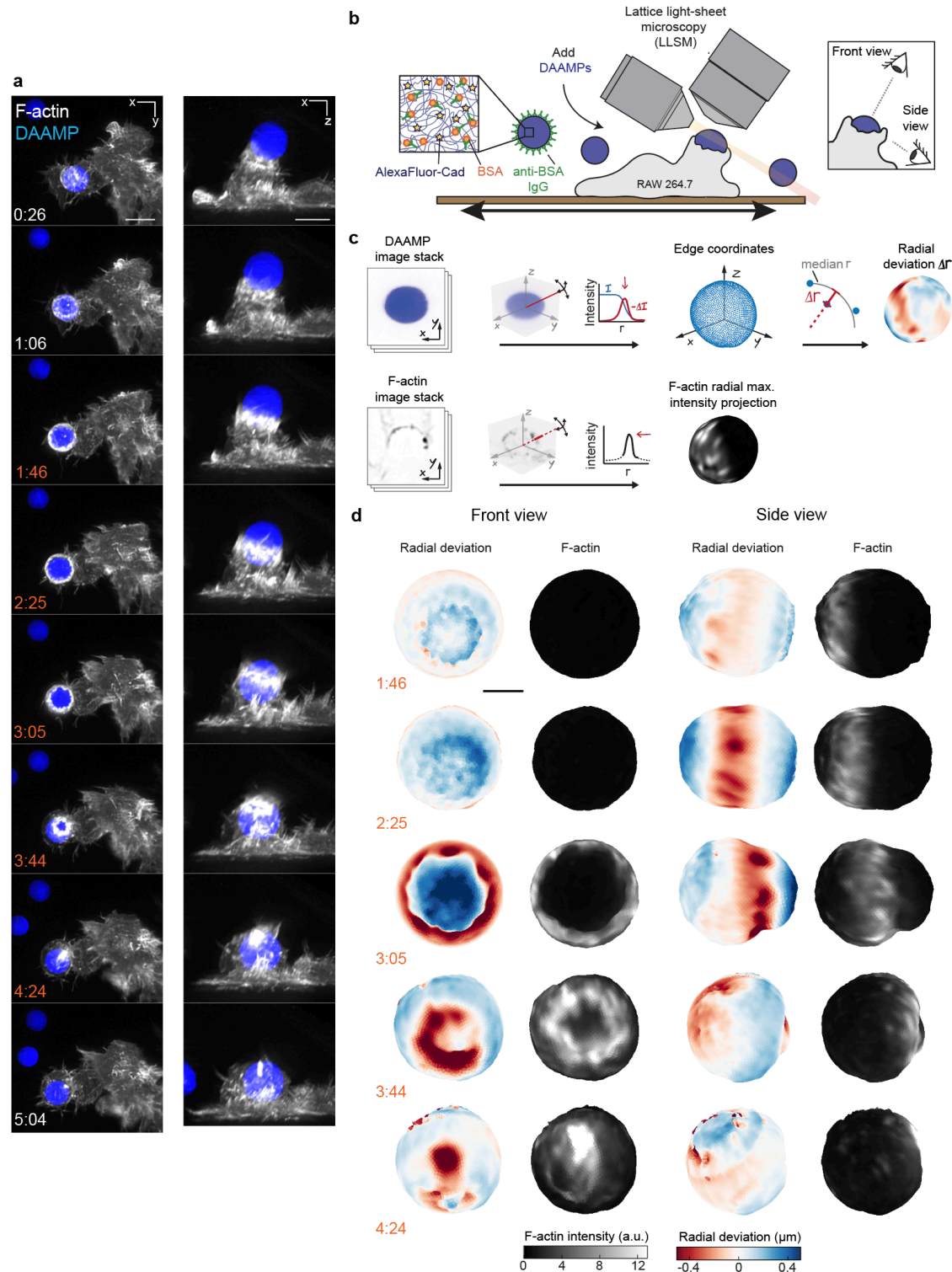
617

Figure 1. **Combined MP-TFM and LLSM reveals phagocytic force-induced deformations in real time.** RAW macrophages transfected with mEmerald-Lifeact were fed DAAM-particles (9 μm,1.4 kPa) functionalized with AF647-Cadaverine, BSA and anti-BSA IgG and imaged using

621   lattice light-sheet microscopy (LLSM). **a,** Time lapse montage (min:s) of maximum intensity

622   projections in x/y and x/z. Scale bar, 5 μm **b,c** Schematic of the combined LLSM and MP-TFM

623   experimental approach and analysis, respectively. **d,** Front and side view of reconstructed DAAM-

624   particle internalized in **a** showing target deformations and F-actin localization on particle surface.

625   Colorscale represents the deviation of each vertex from a perfect sphere with radius equal to the

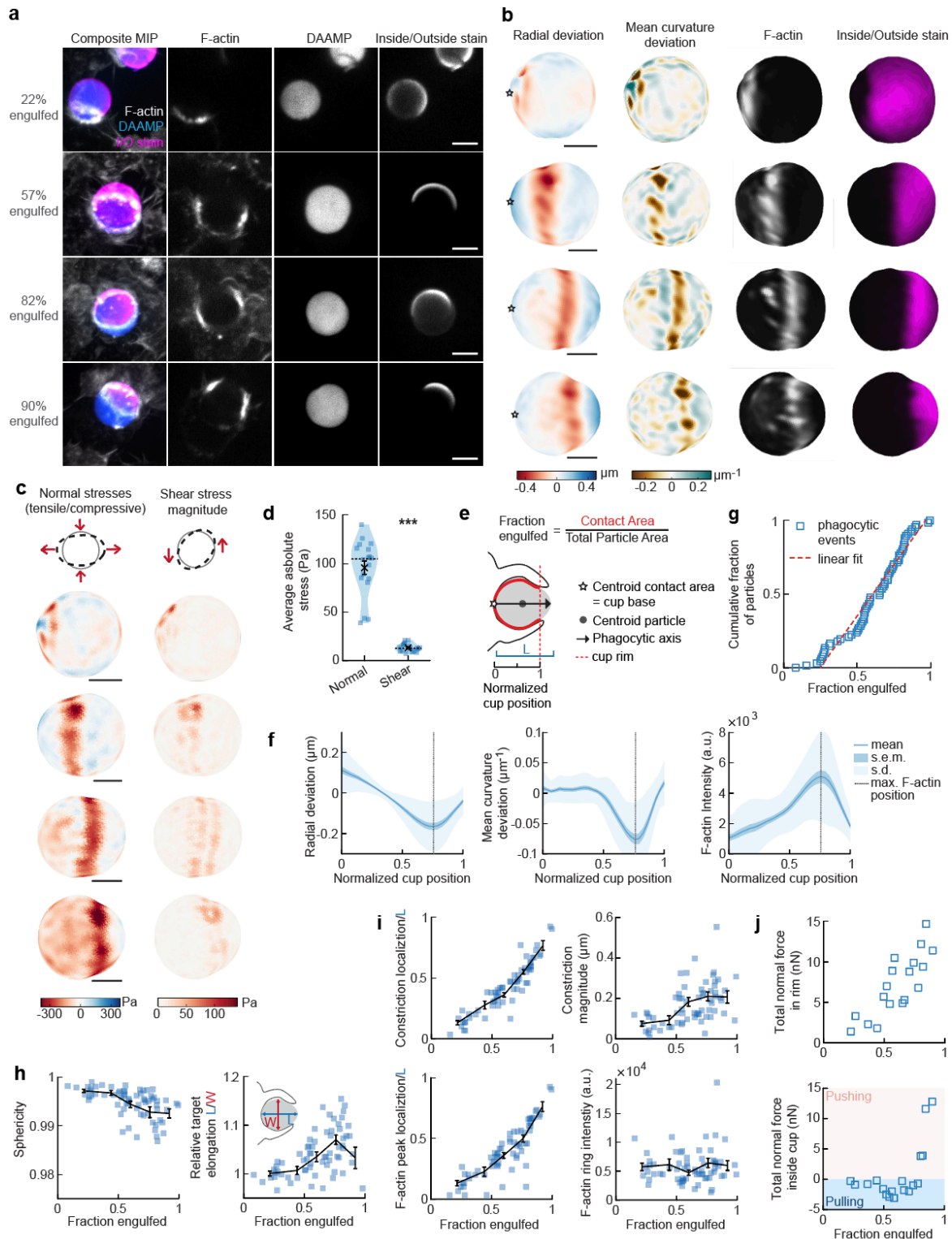626   median radial distance of all edge coordinates to the particle centroid. Scale bar, 3 μm.

Figure 2. Phagocytic forces include strong actin-mediated constriction and increase with phagocytic progression. a, Confocal images of fixed RAW macrophages phagocytosing DAAM-particles functionalized with AF488-Cadaverine, BSA and anti-BSA IgG. Cells were stained for F-

631   actin, and particles with a fluorescent secondary antibody to reveal the exposed surface. Left

632   column: composite maximum intensity projections (MIP) of confocal z-stacks, 2nd to 4th column:

633   single confocal slices through particle centroid. Scale bar, 5 μm. **b,** 3D shape reconstructions of

634   particle in **a** revealing detailed target deformations and localization of F-actin over the particle

635   surface. Scale bars are 3 μm. Stars mark the base of the phagocytic cup, and the phagocytic axis

636   is horizontal (see **e**). **c,** Normal and shear stresses exerted on the targets in **a,b**. Negative normal

637   forces denote (inward) compressive forces. **d,** Averages of absolute magnitudes of compressive

638   and shear stresses for 18 phagocytic cups spread over various stages of engulfment. Violin plots

639   show individual phagocytic events (blue markers), mean (black cross) and median (dashed line).

640   *Two-side Wilcoxon rank sum test: p = 2.0×10^{-4}. **e,** Schematic representation of phagocytic

641   parametrization. Normalized cup position indicates the position along the phagocytic axis relative

642   to the rim of the cup, with 0 the cup base and 1 the rim of the phagocytic cup regardless of

643   engulfment stage. **f,** Average deformation and F-actin intensity profiles along the phagocytic axis

644   to the cup rim. Signals were first processed on a per-particle basis by averaging over the surface

645   along the phagocytic targets in 30 bins. Targets beyond 40% engulfment were included (54 out

646   of 68 events in total). **g**, Cumulative distribution function of the engulfment stage of randomly

647   selected phagocytic events (n = 68). Dashed red line indicates a linear fit. **h,** Target sphericity and

648   elongation depend on phagocytic stage. Blue squares indicate individual measurements, black

649   lines indicate averages within 5 bins. Middle graph inset schematic shows how relative elongation

650   was determined. **i,** Analysis of particle deformation and F-actin fluorescence along the phagocytic

651   axis for all phagocytic events (n = 68). Marker and line styles as in **h**. All error bars indicate s.e.m.

652   unless indicated otherwise. **j,** Analysis of forces in the contractile ring at the cup rim and

653   throughout the remainder of the cup for 18 cups selected for force analysis.
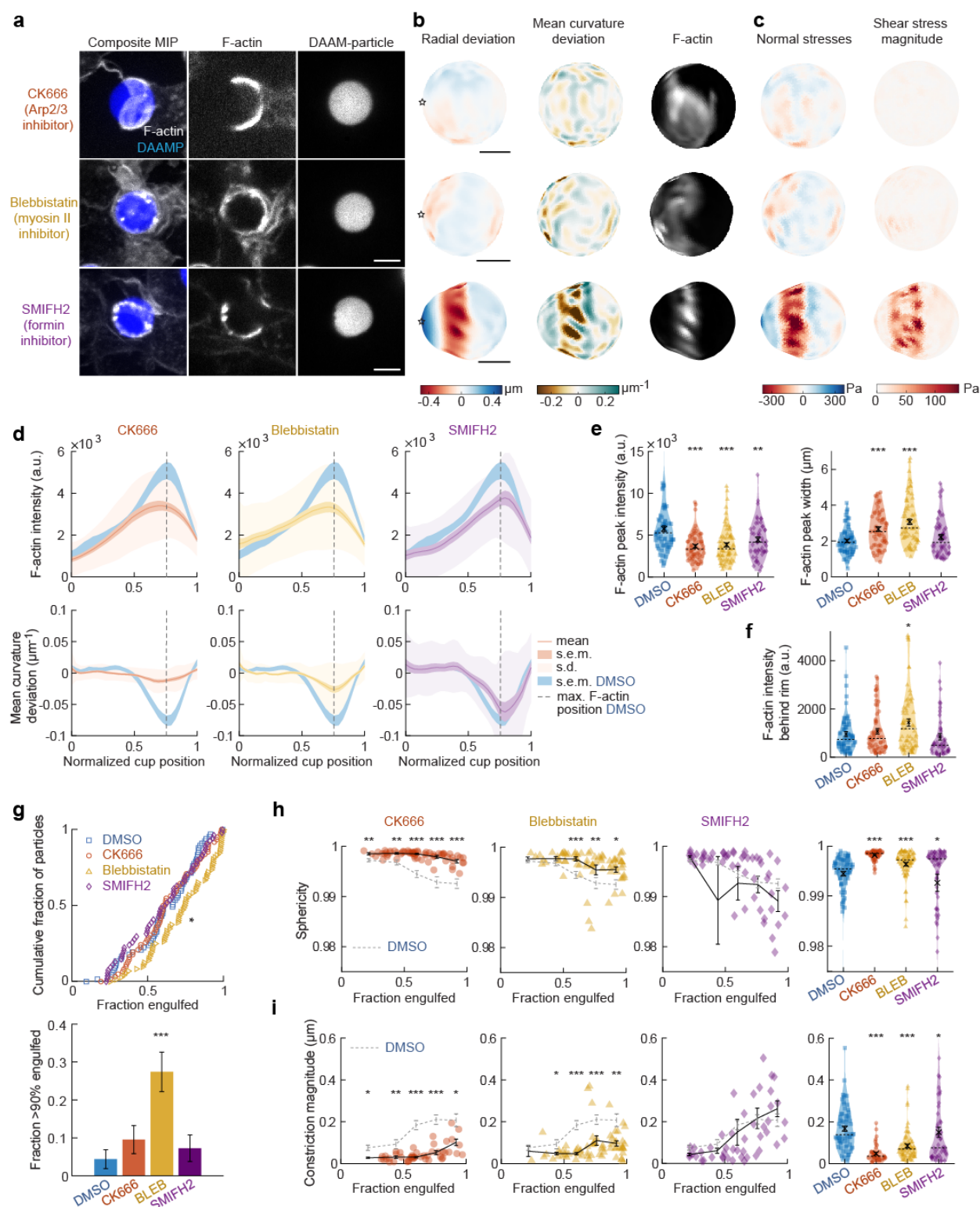
654

Figure 3: Arp2/3-mediated actin polymerization and myosin-II have distinct roles in phagocytic force generation and progression. a, Confocal images of drug-treated fixed RAW cells phagocytosing DAAM-particles functionalized with AF488-Cadaverine, BSA and anti-BSA

659   IgG. Cells were treated with DMSO, CK666 (150 μM), Blebbistatin (15 μM) and SMIFH2 (10 μM)

660   for 30 minutes prior to phagocytic challenge. Each target is approximately 60% engulfed. Fixed

661   cells were stained for F-actin, and particles were labelled with a fluorescent secondary antibody

662   to reveal the exposed surface. Left column: composite maximum intensity projections (MIP) of

663   confocal z-stacks, 2nd-3rd column: single confocal slices through particle centroid. Scale bar, 5

664   μm. **b,** Particle shape reconstructions from **a,** revealing detailed target deformations and

665   localization of F-actin over the particle surface. Stars mark the base of the phagocytic cup, and

666   the phagocytic axis is horizontal. Scale bars, 3 μm. **c,** Normal and shear stresses exerted on the

667   target. Negative normal forces denote (inward) compressive forces. **d,** Average deformation and

668   F-actin intensity profiles along the phagocytic axis to the cup rim. Signals were first processed on

669   a per-particle basis by averaging over the surface along the phagocytic targets in 30 bins. Targets

670   before 40% engulfment were excluded. **e, f,** Violin plots of all measured particles, showing

671   individual phagocytic events (colored markers), mean (black cross) and median (dashed line). **e**,

672   F-actin peak intensity and width. **f**, F-actin intensity in the cup (behind the rim), measured right (3

673   μm) behind the main peak for each particle. **g,** Upper panel, cumulative distribution function of

674   the engulfment stage of randomly selected phagocytic events (n = 68, 63, 73 & 55 respectively)

675   from 3 independent experiments. Two sample Kolmogorov-Smirnov test was used (p = 0.016*).

676   Lower panel, fraction late-stage cups. Error bars indicate st.d. estimated by treating phagocytosis

677   as a Bernoulli process. Fisher's exact test was used to compare fractions (p = $1.9{\times}10^{-4}$)***. **h,**

678   Sphericity and **i**, constriction magnitude of DAAM particle changes with phagocytic progression

679   upon drug treatment. Colored markers indicate individual events, black lines indicate averages

680   within 5 bins. Right column, violin plots of all events. Marker and line styles as in **e**. All statistical

681   tests were two-side Wilcoxon rank sum test comparing with the DMSO control (gray) over the

682   same bin with significance levels: p < 0.05*; p < 0.01**; p < 0.001***, unless otherwise indicated.

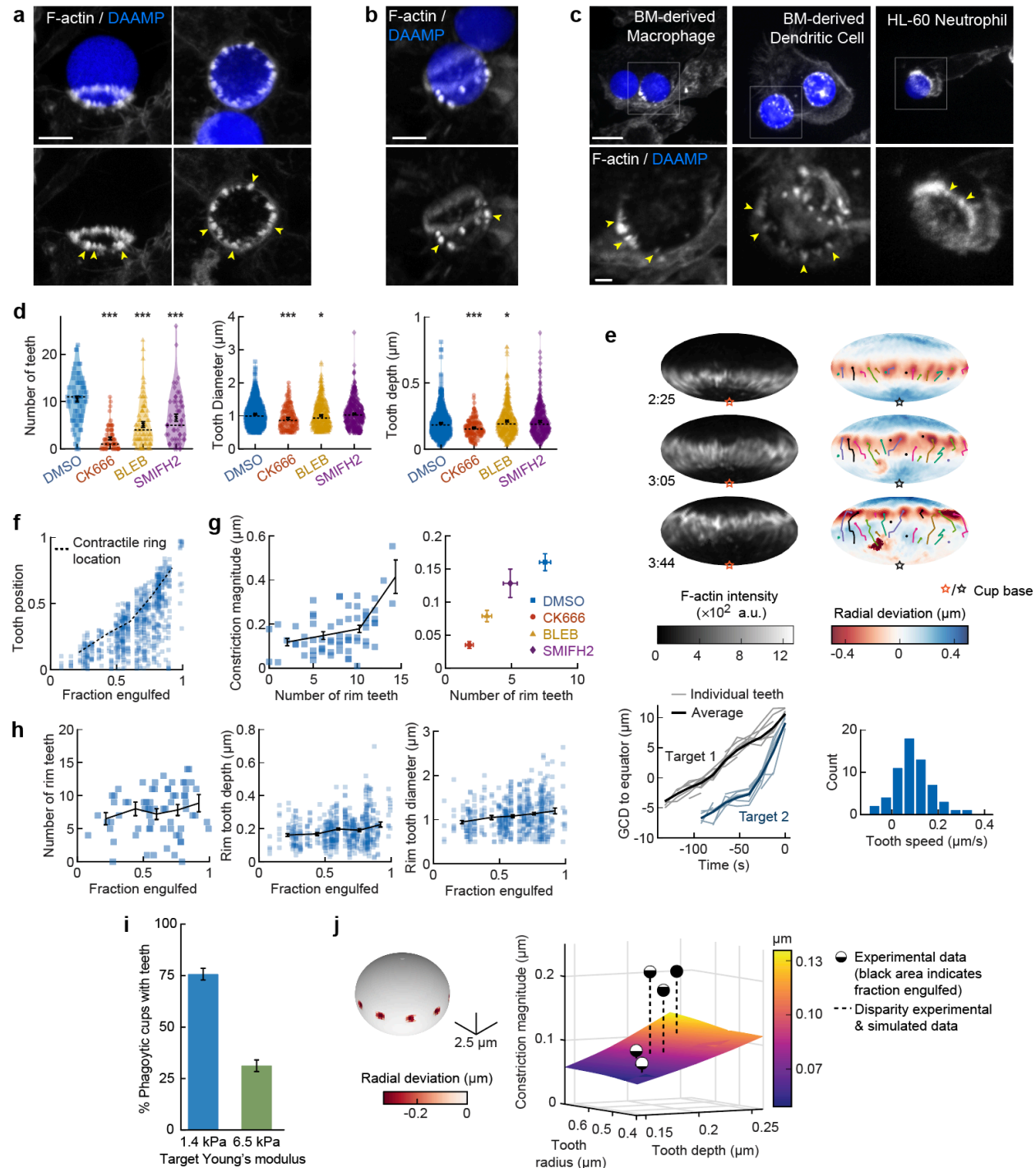683   All error bars indicate s.e.m. unless indicated otherwise.

Figure 4. Actin-based teeth are dynamic interconnected structures whose protrusive activity contributes to target constriction. **a**,**b,** RAW macrophages were fed 1.4 kPa DAAMPs and stained for F-actin. Images represent maximum intensity projections of confocal Z-stacks. Yellow arrows point to actin-based "teeth". **a,** representative images of teeth at the rim of the phagocytic cup deforming the target. Scale bar, 5 μm. **b,** Example of actin-based teeth observed

690   within the phagocytic cup. Scale bar, 5 μm. **c,** Primary murine bone-marrow derived macrophage

691   (BMDM), as well as primary bone-marrow derived dendritic cell (BMDC) and HL-60 neutrophil-

692   like cells also form actin teeth in response to DAAMP internalization. Scale bar, 5 μm. zoom scale

693   bar, 2 μm. **d,** CK666, blebbistatin, and SMIFH2 treatments reduce formation of actin-based teeth

694   within the phagocytic cup. Teeth size and shape are also modestly affected. Violin plots with

695   individual particles (colored markers), means (black cross), median (dashed line) **e,** Manually

696   tracked actin teeth trajectories from DAAMP internalization imaged by LLSM. Particle surface is

697   shown using Mollweide projection (Supplementary Fig. 2c). Three timepoints of a single

698   phagocytic event are shown, with different colors representing unique teeth. Circles indicate

699   current or final position of a tracked tooth. Lines connect the previous positions of tracked teeth.

700   Lower left; great circle distance (GCD) of teeth to the equator for 2 events. Target one is visualized

701   above, time 0 corresponds to the time at which engulfment was completed. Lower right;

702   distribution of tooth speeds with average 0.094 ± 0.08 μm/s (= 5.6 μm/min) from 3 phagocytic

703   events (60 teeth in total from target 1& 2 in this panel, and from Supplementary Fig. 7d). Tooth

704   speeds were averaged over the trajectory of individual teeth. **f,** Teeth are mostly located at the

705   rim of the cup. Markers represent individual teeth (n = 716) **g,** Constriction magnitude correlates

706   with the number of teeth with Spearman's rank correlation coefficient (r) = 0.42 (p = $4.4*10^{-4}$) for

707   individual DMSO phagocytic events (left) and between drug treatments (right). **h,** Teeth number

708   and features change with phagocytic progression, with, from left to right, r = 0.2 (p = 0.11 n.s.), r

709   = 0.17 (p = $1.0×10^{-4}$), r = 0.16 (p = $2.1×10^{-4}$). **i,** Phagocytic cups with actin teeth appear more

710   frequently when cells are challenged with softer targets. RAW macrophages were challenged with

711   9 μm DAAMPs of 1.4 kPa or 6.5 kPa, fixed and stained for F-actin. **j,** Elasticity theory simulations

712   of the relation between tooth size and depth and overall constriction magnitude. Inset shows teeth,

713   simulated as spherical indenters on a spherical target. Bar graph represents pooled data (n =

714   >150 cups) from 3 independent experiments. Error bars indicate st.d. estimated by treating

715   phagocytosis as a Bernoulli process. Pooled data was compared using Fisher's exact test to

716   compare fractions (p = $1.5×10^{-24}$***). All error bars indicate s.e.m unless otherwise indicated.
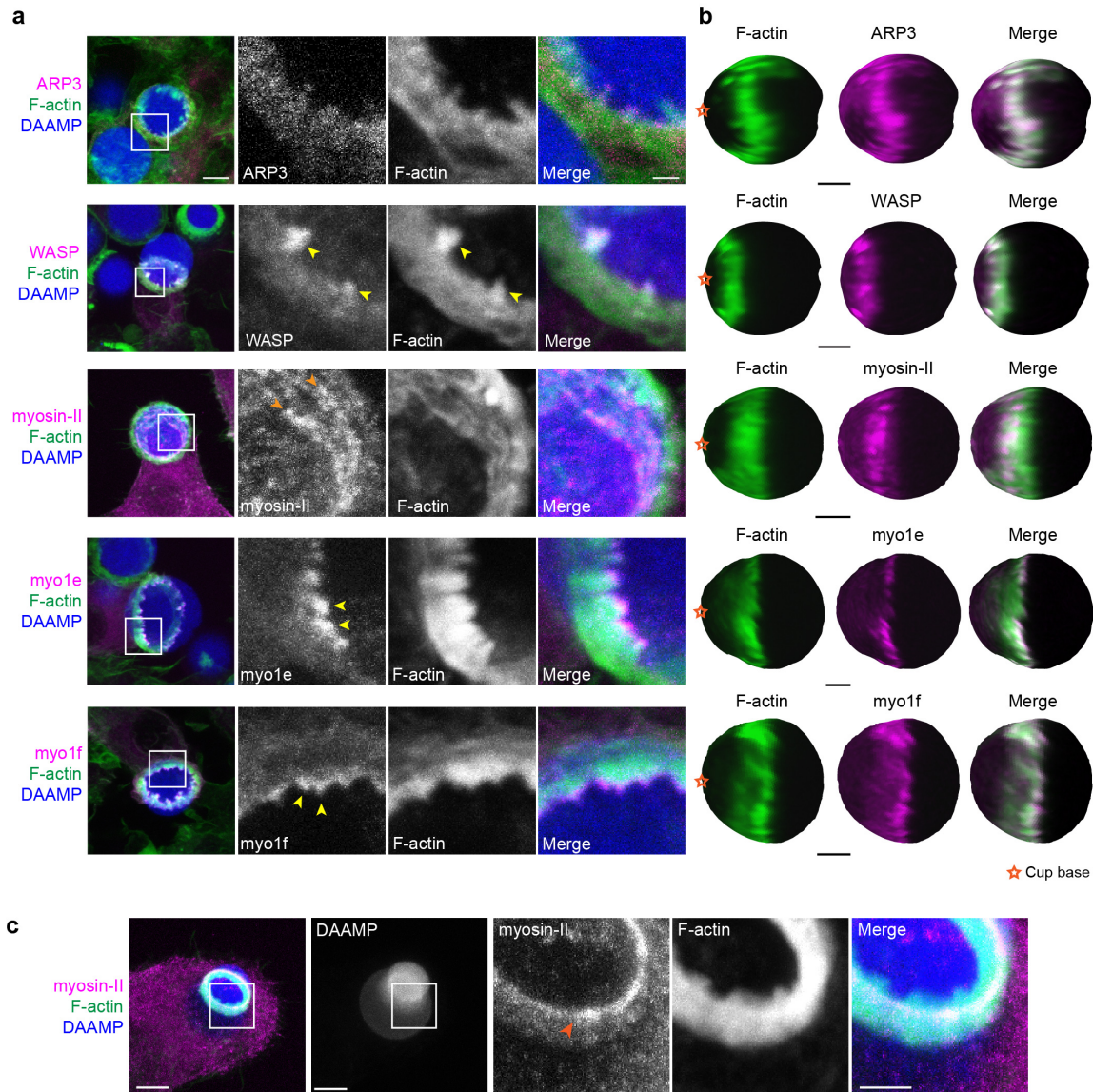
Figure 5. Multiple actin regulatory proteins localize to phagocytic teeth. **a,** RAW macrophages were transfected with fluorescently tagged actin binding proteins and challenged to ingest DAAMPs (11 μm, 1.4 kPa) functionalized with AF647-Cadaverine, BSA and anti-BSA IgG to assess localization to actin teeth (yellow arrowheads). Images are maximum intensity projections of confocal Z-stacks. White boxes in leftmost panels indicate the site of the zoomed images to the right. Scale bar, 5 μm. Zoom scale bar, 1 μm. **b,** DAAM-particle reconstructions for examples shown in **a,** showing target deformations and localization of fluorescent proteins with respect to actin teeth. Scale bar, 3 μm. **c,** Myosin-II condensing into thick concentric rings (marked by orange arrowheads) during late-stage phagocytosis of a highly deformed target. Images are maximum intensity projections of confocal Z-stacks. Scale bar, 5 μm. Zoom scale bar, 1 μm.
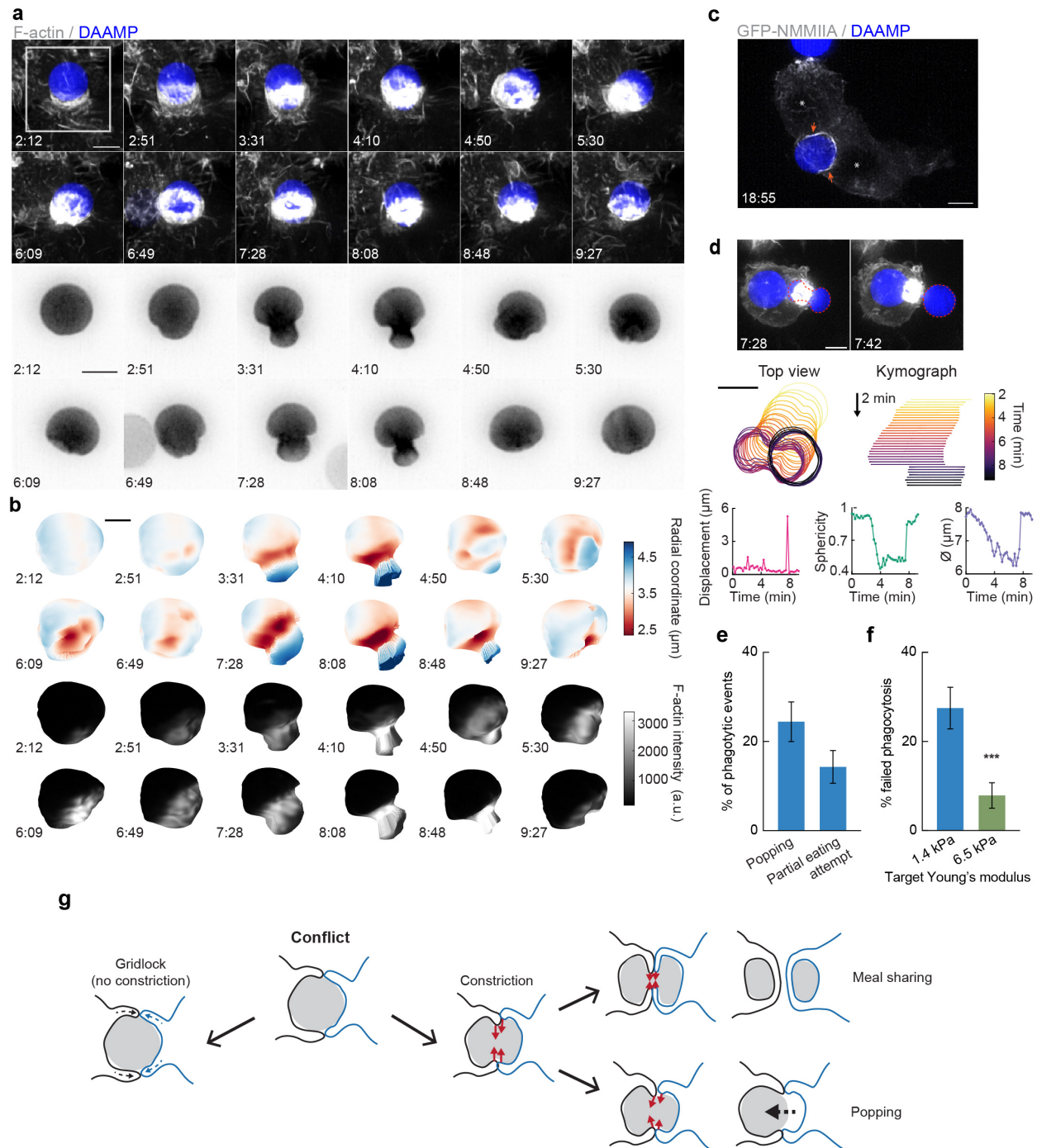
30

Figure 6. Contractile activity may enable resolving conflicts by partial target eating and a popping release mechanism. a, Maximum intensity projections (MIP) of LLSM stacks showing failed internalization attempt of RAW macrophage with IgG-functionalized 1.4 kPa DAAMP. Zoomed images of the area marked by the white box showing only the DAAMP channel (inverse grayscale LUT) are shown below. **b,** 3D reconstructions showing both the particle shape and F-actin signal over the particle surface corresponding to the event in **a**. Scale bar, 3 μm. **c,** MIP of

735   LLSM stacks showing myosin-II accumulation (orange arrows) during a partial eating event. RAW

736   macrophages (marked by *) were transfected with EGFP-NMMIIA and challenged with IgG-

737   functionalized 1.4 kPa DAAMP. **d**, Top: MIPs of LLSM stacks of RAW macrophage suddenly

738   releasing heavily deformed target. Red dashed line outlines DAAMP. Middle, particle position and

739   outline (left), and kymograph of particle position (right). Bottom, Particle displacement, sphericity

740   and apparent diameter over time of the same event shows the sudden nature of the release. **e,**

741   Sudden forfeit by a popping mechanism and attempted partial eating are common for 1.4 kPa

742   targets, with ~24% and ~14% occurrence of all phagocytic events, respectively. **f,** Percentage of

743   failed phagocytic events is dependent on particle rigidity. Data from 2-4 independent experiments

744   was pooled (n = 89, 91 phagocytic events) and compared using Fisher's exact test (p = 7.4×10^{-4}

745   ). **g,** Schematic representation of the multiple ways in which target constriction may enable

746   resolving macrophage conflicts in which two cells attempt a single target. All scale bars are 5 μm,

747   unless otherwise indicated. All error bars indicate s.d. estimated by treating phagocytosis as a
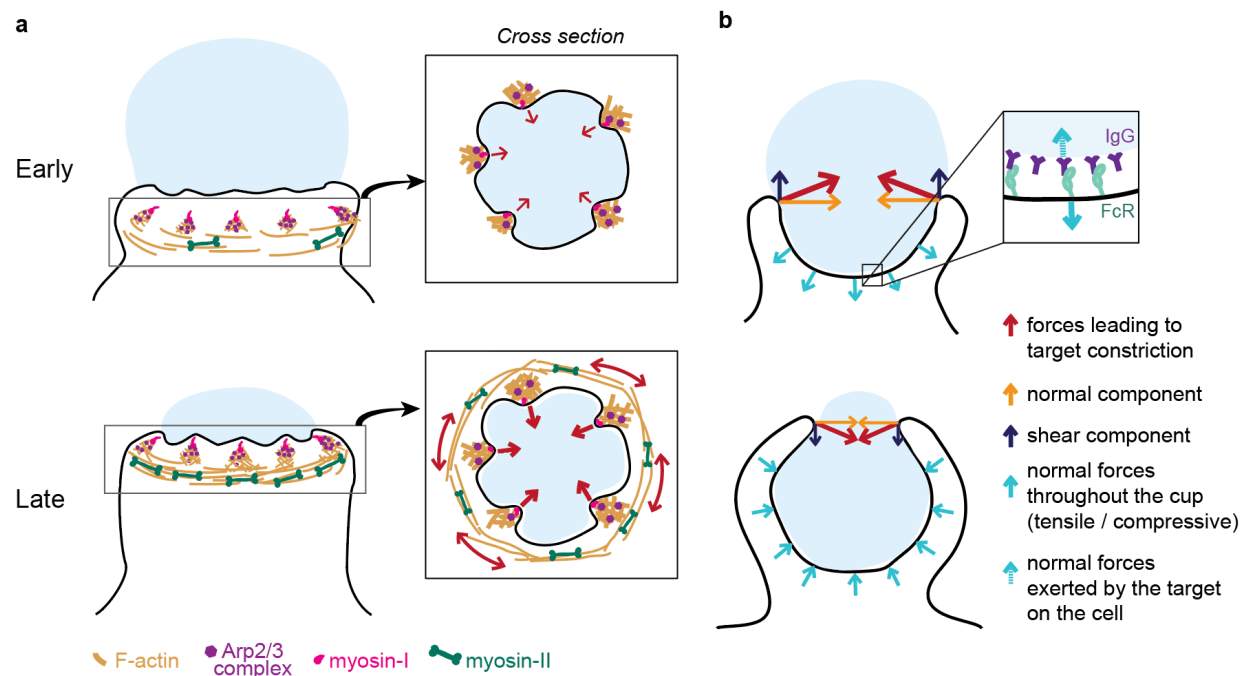
748   Bernoulli process.

32

749

Figure 7. Model of the molecular players and force balance during phagocytosis. a, Graphical model: Arp2/3 mediated actin teeth, guided by myosin-I motors, and organized in a ring drive phagocytic progression and inward target deformation. Teeth are interconnected through myosin-II filaments located behind the actin teeth. **b,** Ring-like target constriction by protrusive actin teeth and myosin II activity (red arrows) can be decomposed in forces orthogonal to the phagocytic axis, which are balanced within the ring (yellow arrows) and along the phagocytic axis, which result in a net force exerted by the ring (purple arrows). The local target geometry at the protruding rim of the cup determines the direction of the net force. Before 50% engulfment, this force points outward and is balanced by pulling forces throughout the base of the phagocytic cup (push and lock). Inset, the pulling forces from the cell (dashed arrow) on the target and paired forces from the target on the cell (solid arrow) likely put the receptor-ligand interactions under tension. After 50% engulfment, the net ring force points inward, and is balanced by compressive forces (cyan arrows) throughout the phagocytic cup.

33

References

763

764   1.   Lim, J. J., Grinstein, S. & Roth, Z. Diversity and Versatility of Phagocytosis: Roles in
765   Innate Immunity, Tissue Remodeling, and Homeostasis. *Front. Cell. Infect. Microbiol.* **7**,
766   1–12 (2017).

767   2.   Boada-Romero, E., Martinez, J., Heckmann, B. L. & Green, D. R. The clearance of dead
768   cells by efferocytosis. *Nat. Rev. Mol. Cell Biol.* **21**, 398–414 (2020).

769   3.   Uribe-Querol, E. & Rosales, C. Phagocytosis: Our Current Understanding of a Universal
770   Biological Process. *Front. Immunol.* **11**, 1–13 (2020).

771   4.   Freeman, S. A. & Grinstein, S. Phagocytosis: receptors, signal integration, and the
772   cytoskeleton. *Immunol. Rev.* **262**, 193–215 (2014).

773   5.   Griffin, F. M. & Silverstein, S. C. Segmental Response of the Macrophage Plasma
774   Membrane to a Phagocytic Stimulus. *J. Exp. Med.* **139**, 323–336 (1974).

775   6.   Swanson, J. A. & Hoppe, A. D. The coordination of signaling during Fc receptor-mediated
776   phagocytosis. *J. Leukoc. Biol.* **76**, 1093–1103 (2004).

777   7.   Jaumouillé, V. & Waterman, C. M. Physical Constraints and Forces Involved in
778   Phagocytosis. *Front. Immunol.* **11**, 1–20 (2020).

779   8.   Vorselen, D., Labitigan, R. L. D. & Theriot, J. A. A mechanical perspective on phagocytic
780   cup formation. *Curr. Opin. Cell Biol.* **66**, 112–122 (2020).

781   9.   Blanchoin, L., Boujemaa-Paterski, R., Sykes, C. & Plastino, J. Actin Dynamics,
782   Architecture, and Mechanics in Cell Motility. *Physiol. Rev.* **94**, 235–263 (2014).

783   10. Small, J. V., Stradal, T., Vignal, E. & Rottner, K. The lamellipodium: where motility begins.
784   *Trends Cell Biol.* **12**, 112–120 (2002).

785   11. Davidson, A. J. & Wood, W. Macrophages Use Distinct Actin Regulators to Switch
786   Engulfment Strategies and Ensure Phagocytic Plasticity In Vivo. *Cell Rep.* (2020).
787   doi:10.1016/j.celrep.2020.107692

788   12. Barger, S. R. *et al.* Membrane-cytoskeletal crosstalk mediated by myosin-I regulates
789   adhesion turnover during phagocytosis. *Nat Commun* **10**, 1249 (2019).

790   13. Ostrowski, P. P., Freeman, S. A., Fairn, G. & Grinstein, S. Dynamic Podosome-Like
791   Structures in Nascent Phagosomes Are Coordinated by Phosphoinositides. *Dev. Cell* **50**,
792   397-410.e3 (2019).

793   14. Linder, S. The matrix corroded: podosomes and invadopodia in extracellular matrix
794   degradation. *Trends Cell Biol.* **17**, 107–117 (2007).

795   15. van den Dries, K., Linder, S., Maridonneau-Parini, I. & Poincloux, R. Probing the
796   mechanical landscape – new insights into podosome architecture and mechanics. *J. Cell
797   Sci.* **132**, jcs236828 (2019).

798   16. Labernadie, A. *et al.* Protrusion force microscopy reveals oscillatory force generation and
799   mechanosensing activity of human macrophage podosomes. *Nat. Commun.* **5**, 5343
800   (2014).

801   17. van den Dries, K. *et al.* Modular actin nano-architecture enables podosome protrusion
802   and mechanosensing. *Nat. Commun.* **10**, 1–16 (2019).

803   18.   Beningo, K. A. & Wang, Y. Fc-receptor-mediated phagocytosis is regulated by
804   mechanical properties of the target. *J. Cell Sci.* **115**, 849–56 (2002).

805   19.   Sosale, N. G. *et al.* Cell rigidity and shape override CD47's 'self'-signaling in
806   phagocytosis by hyperactivating myosin-II. *Blood* **125**, 542–552 (2015).

807   20.   Jaumouillé, V., Cartagena-Rivera, A. X. & Waterman, C. M. Coupling of β2 integrins to
808   actin by a mechanosensitive molecular clutch drives complement receptor-mediated
809   phagocytosis. *Nat. Cell Biol.* **21**, 1357–1369 (2019).

810   21.   Vorselen, D. *et al.* Microparticle traction force microscopy reveals subcellular force
811   exertion patterns in immune cell–target interactions. *Nat. Commun.* **11**, 20 (2020).

812   22.   Swanson, J. A. *et al.* A contractile activity that closes phagosomes in macrophages. *J.
813   Cell Sci.* **112 (Pt 3**, 307–16 (1999).

814   23.   Araki, N., Hatae, T., Furukawa, A. & Swanson, J. A. Phosphoinositide-3-kinase-
815   independent contractile activities associated with Fcgamma-receptor-mediated
816   phagocytosis and macropinocytosis in macrophages. *J Cell Sci* **116**, 247–257 (2003).

817   24.   Ikeda, Y. *et al.* Rac1 switching at the right time and location is essential for Fcγ receptor-
818   mediated phagosome formation. *J. Cell Sci.* **130**, 2530–2540 (2017).

819   25.   Kovari, D. T. *et al.* Frustrated Phagocytic Spreading of J774A-1 Macrophages Ends in
820   Myosin II-Dependent Contraction. *Biophys. J.* **111**, 2698–2710 (2016).

821   26.   Barger, S. R., Gauthier, N. C. & Krendel, M. Squeezing in a Meal: Myosin Functions in
822   Phagocytosis. *Trends Cell Biol.* **30**, 157–167 (2020).

823   27.   Rotty, J. D. *et al.* Arp2/3 Complex Is Required for Macrophage Integrin Functions but Is
824   Dispensable for FcR Phagocytosis and In Vivo Motility. *Dev. Cell* **42**, 498-513.e6 (2017).

825   28.   Olazabal, I. M. *et al.* Rho-kinase and myosin-II control phagocytic cup formation during
826   CR, but not FcgammaR, phagocytosis. *Curr Biol* **12**, 1413–1418 (2002).

827   29.   Heinrich, V. Controlled One-on-One Encounters between Immune Cells and Microbes
828   Reveal Mechanisms of Phagocytosis. *Biophys. J.* **109**, 469–476 (2015).

829   30.   Herant, M. Mechanics of neutrophil phagocytosis: behavior of the cortical tension. *J. Cell
830   Sci.* **118**, 1789–1797 (2005).

831   31.   Rougerie, P. & Cox, D. Spatio-temporal mapping of mechanical force generated by
832   macrophages during FcγR-dependent phagocytosis reveals adaptation to target stiffness.
833   *bioRxiv* (2020). doi:10.1101/2020.04.14.041335

834   32.   Mohagheghian, E. *et al.* Quantifying compressive forces between living cell layers and
835   within tissues using elastic round microgels. *Nat. Commun.* **9**, 1878 (2018).

836   33.   Träber, N. *et al.* Polyacrylamide Bead Sensors for in vivo Quantification of Cell-Scale
837   Stress in Zebrafish Development. *Sci. Rep.* **9**, 17031 (2019).

838   34.   Horsthemke, M. *et al.* Multiple roles of filopodial dynamics in particle capture and
839   phagocytosis and phenotypes of Cdc42 and Myo10 deletion. *J. Biol. Chem.* **292**, 7258–
840   7273 (2017).

841   35.   Freeman, S. A. *et al.* Lipid-gated monovalent ion fluxes regulate endocytic traffic and
842   support immune surveillance. *Science (80-.).* (2020). doi:10.1126/science.aaw9544

843 36. Liebl, D. & Griffiths, G. Transient assembly of F-actin by phagosomes delays phagosome
844   fusion with lysosomes in cargo-overloaded macrophages. *J. Cell Sci.* (2009).
845   doi:10.1242/jcs.048355

846 37. Legant, W. R. *et al.* Multidimensional traction force microscopy reveals out-of-plane
847   rotational moments about focal adhesions. *Proc. Natl. Acad. Sci.* **110**, 881–886 (2013).

848 38. Case, L. B. & Waterman, C. M. Integration of actin dynamics and cell adhesion by a
849   three-dimensional, mechanosensitive molecular clutch. *Nat. Cell Biol.* **17**, 955–963
850   (2015).

851 39. van Zon, J. S., Tzircotis, G., Caron, E. & Howard, M. A mechanical bottleneck explains
852   the variation in cup growth during FcgammaR phagocytosis. *Mol. Syst. Biol.* **5**, 298
853   (2009).

854 40. Wilson, C. A. *et al.* Myosin II contributes to cell-scale actin network treadmilling through
855   network disassembly. *Nature* **465**, 373–377 (2010).

856 41. Ostrowski, P. P., Freeman, S. A., Fairn, G. & Grinstein, S. Dynamic Podosome-Like
857   Structures in Nascent Phagosomes Are Coordinated by Phosphoinositides. *Dev. Cell* **50**,
858   397-410.e3 (2019).

859 42. Proag, A. *et al.* Working together: Spatial synchrony in the force and actin dynamics of
860   podosome first neighbors. *ACS Nano* **9**, 3800–3813 (2015).

861 43. Meddens, M. B. M. *et al.* Actomyosin-dependent dynamic spatial patterns of cytoskeletal
862   components drive mesoscale podosome organization. *Nat. Commun.* **7**, 1–17 (2016).

863 44. Greenberg, S., Burridge, K. & Silverstein, S. C. Colocalization of F-actin and talin during
864   Fc receptor-mediated phagocytosis in mouse macrophages. *J Exp Med* **172**, 1853–1856
865   (1990).

866 45. Herant, M., Heinrich, V. & Dembo, M. Mechanics of neutrophil phagocytosis: experiments
867   and quantitative models. *J. Cell Sci.* **119**, 1903–13 (2006).

868 46. Tollis, S., Dart, A. E., Tzircotis, G. & Endres, R. G. The zipper mechanism in
869   phagocytosis: energetic requirements and variability in phagocytic cup shape. *BMC Syst.*
870   *Biol.* **4**, 149 (2010).

871 47. Matlung, H. L. *et al.* Neutrophils Kill Antibody-Opsonized Cancer Cells by Trogoptosis.
872   *Cell Rep.* **23**, 3946-3959.e6 (2018).

873 48. Velmurugan, R., Challa, D. K., Ram, S., Ober, R. J. & Ward, E. S. Macrophage-mediated
874   trogocytosis leads to death of antibody-opsonized tumor cells. *Mol. Cancer Ther.* **15**,
875   1879–1889 (2016).

876 49. Morrissey, M. A. *et al.* Chimeric antigen receptors that trigger phagocytosis. *Elife* **7**,
877   e36688 (2018).

878 50. Walbaum, S. *et al.* Complement receptor 3 mediates both sinking phagocytosis and
879   phagocytic cup formation via distinct mechanisms. *J. Biol. Chem.* **296**, 100256 (2021).

880 51. Hoijman, E. *et al.* Cooperative epithelial phagocytosis enables error correction in the early
881   embryo. *Nature* **590**, 618–623 (2021).

882 52. Bieling, P. *et al.* Force Feedback Controls Motor Activity and Mechanical Properties of
883   Self-Assembling Branched Actin Networks. *Cell* **164**, 115–127 (2016).

884 53. Marie-Anaïs, F., Mazzolini, J., Bourdoncle, P. & Niedergang, F. 'Phagosome Closure
885   Assay' to Visualize Phagosome Formation in Three Dimensions Using Total Internal
886   Reflection Fluorescent Microscopy (TIRFM). *J. Vis. Exp.* **2016**, 1–8 (2016).

887 54. Nishi, H. *et al.* Neutrophil FcγRIIA promotes IgG-mediated glomerular neutrophil capture
888   via Abl/Src kinases. *J. Clin. Invest.* **127**, 3810–3826 (2017).

889 55. Zhu, C., Chen, W., Lou, J., Rittase, W. & Li, K. Mechanosensing through
890   immunoreceptors. *Nat. Immunol.* **20**, 1269–1278 (2019).

891 56. Schuerle, S. *et al.* Robotically controlled microprey to resolve initial attack modes
892   preceding phagocytosis. *Sci. Robot.* **2**, eaah6094 (2017).

893 57. Champion, J. A. & Mitragotri, S. Role of target geometry in phagocytosis. *Proc. Natl.
894   Acad. Sci. U. S. A.* **103**, 4930–4 (2006).

895 58. Bakalar, M. H. *et al.* Size-Dependent Segregation Controls Macrophage Phagocytosis of
896   Antibody-Opsonized Targets. *Cell* **174**, 131-142.e13 (2018).

897 59. Colucci-Guyon, E., Tinevez, J.-Y., Renshaw, S. A. & Herbomel, P. Strategies of
898   professional phagocytes in vivo: unlike macrophages, neutrophils engulf only surface-
899   associated microbes. *J. Cell Sci.* **124**, 3053–3059 (2011).

900 60. Gosavi, R. A. *et al.* Optimization of Ex Vivo Murine Bone Marrow Derived Immature
901   Dendritic Cells: A Comparative Analysis of Flask Culture Method and Mouse CD11c
902   Positive Selection Kit Method . *Bone Marrow Res.* (2018). doi:10.1155/2018/3495086

903 61. Chen, B. C. *et al.* Lattice light-sheet microscopy: Imaging molecules to embryos at high
904   spatiotemporal resolution. *Science (80-.).* (2014). doi:10.1126/science.1257998

905 62. Rusinkiewicz, S. Estimating curvatures and their derivatives on triangle meshes. in
906   *Proceedings. 2nd International Symposium on 3D Data Processing, Visualization and
907   Transmission, 2004. 3DPVT 2004.* 486–493 (IEEE, 2004).
908   doi:10.1109/TDPVT.2004.1335277

909 63. Ben Shabat, Y. & Fischer, A. Design of Porous Micro-Structures Using Curvature
910   Analysis for Additive-Manufacturing. *Procedia CIRP* **36**, 279–284 (2015).

911 64. Wang, Y., Zhang, X. & Cai, W. Spherical harmonics method for computing the image
912   stress due to a spherical void. *J. Mech. Phys. Solids* **126**, 151–167 (2019).

913 65. Johnson, K. L. *Contact Mechanics*. (Cambridge University Press, 1985).

914 66. Wieczorek, M. A. & Meschede, M. SHTools: Tools for Working with Spherical Harmonics.
915   *Geochemistry, Geophys. Geosystems* **19**, 2574–2592 (2018).

916